| **ARTICLE** OPEN ACCESS

Influence of the Cr to Ti Ratio on the High-Temperature Oxidation Behavior of TaMoCrTiAl Complex Concentrated Alloys in Nitrogen-Free Atmospheres

Fabian Lanoy[1] (iD) | Emma M. H. White[1] (iD) | Bjoern Schäfer[2] | Chongchong Tang[2] | Carsten Schroer[2] | Bronislava Gorr[2] | Mathias C. Galetz[1] (iD)

[1]Dechema-Forschungsinstitut, Theodor-Heuss-Allee 25, Frankfurt, Germany | [2]Karlsruhe Institute of Technology, IAM-AWP, Kaiserstraße 12, Karlsruhe, Germany

Correspondence: Fabian Lanoy (fabian.lanoy@dechema.de)

ABSTRACT

Refractory high-entropy alloys (RHEAs) offer high strength at extreme temperatures but suffer from poor oxidation resistance. The Ta-Mo-Cr-Ti-Al system shows promising oxidation resistance due to protective $(Cr,Ti,Ta)O_2$ scale formation. This study investigates how varying Cr:Ti ratios (2:1, 1:2, and equimolar) affect microstructure and oxidation behavior in Ar-5 vol.%H_2O and Ar-2.5 vol.%O_2 atmospheres at 1000°C. Titanium influences oxide defect structure through its valence state, controlling oxygen transport kinetics. Results demonstrate strong atmosphere-dependent performance: Cr-rich alloys excel in dry oxygen due to continuous chromia formation and reduced oxygen diffusion zones, while Ti-rich alloys perform superior in humid conditions, likely due to hydrogen uptake effects and reduced chromium volatilization. The study reveals that optimal oxidation resistance requires atmosphere-specific compositions, with microstructural factors (Laves phase distribution) playing equally important roles as oxide defect chemistry in determining overall performance.

1 | Introduction

To improve the efficiency and reduce the emission impact of gas turbines, new structural materials that can withstand higher temperatures in harsh environments are required [1]. Unfortunately, elements with a higher melting point than Ni, such as refractory metals like Nb, Ta, or Mo typically have poor oxidation resistance as they do not form protective oxide scales [2, 3]. Refractory high entropy alloys or complex concentrated alloys (CCAs) have recently caught momentum as potential candidates for high temperature structural materials, being able to surpass conventional alloys in strength [4–9], even more at high temperatures [1, 3, 4, 6].

The equimolar system Ta-Mo-Cr-Ti-Al has shown significant oxidation resistance compared to other refractory-rich high-entropy alloys [6, 10, 11]. At temperatures of 1000°C up to 1500°C [3, 11–13], the oxidation resistance of this alloy has been attributed to a thin and continuous $CrTaO_4$ layer forming under a mixed outer oxide scale containing non-continuous chromia, alumina and titania [3, 11, 12, 14, 15]. It was shown that this rutile-type complex oxide contains Ti to form non-stoichiometric $(Cr,Ti,Ta)O_2$, and Ti has a significant influence on the oxidation resistance [14, 16].

The selection of specific Cr:Ti ratios for this investigation is motivated by defect chemistry considerations in the protective $(Cr,Ti,Ta)O_2$ scale. In rutile-structured oxides, the ratios of Cr^{3+}, Ti^{4+}, and Ta^{5+} cations with their respective oxide valences influence the electronic defect structure and oxygen transport properties. It is well-established that rutile-type TiO_2 is susceptible to lattice defects that can either enable or inhibit oxygen diffusion by altering oxygen vacancy concentrations [2, 14, 17–20].

Previous work by Schellert et al. [14] demonstrated that reduced Ti content decreases oxidation resistance. Based on these observations and established defect equilibria in rutile systems, we hypothesize that increased Ti content could improve oxidation resistance through a charge compensation mechanism. Specifically, Ti^{4+} substitution for Cr^{3+} should reduce oxygen vacancy concentrations.

This study aims to clarify the influence of systematic Cr:Ti ratio variations on alloy microstructures and the formation characteristics of $(Cr,Ti,Ta)O_2$ protective scales, with the goal of validating the proposed defect chemistry hypothesis. To test this theoretical framework, three alloys with controlled Cr:Ti variations were investigated: 20Ta-20Mo-27Cr-13Ti-20Al, 20Ta-20Mo-13Cr-27Ti-20Al and 20Ta-20Mo-20Cr-20Ti-20Al (all in at.%), corresponding to Cr:Ti ratios of 2:1, 1:2, and 1:1, respectively.

The experimental design ensures that only Cr and Ti concentrations vary systematically while the contents of Ta, Mo, and Al remain constant, allowing for direct assessment of Cr:Ti ratio effects on oxidation behavior. By examining the oxidation performance under different atmospheric conditions, this approach enables separation of defect chemistry effects from microstructural and environmental influences on oxidation resistance.

2 | Experimental Procedures

2.1 | Sample Manufacturing

The sample material used was manufactured by arc melting (Edmund Bühler AM500) using high-purity ($\geq$ 99.9%) raw materials (Haines-Maassen: Ta & Al; GfE: Ti; Plansee: Mo; QUKEN New Material: Cr) in argon. Following the alloying process, the microstructure of the samples was homogenized to dissolve the dendritic microstructure resulting from fast directional solidification in the water-cooled copper mold. Homogenization was performed at 1500°C for 20 h in a tube furnace in flowing argon, the nominal compositions of the sample materials are shown in Table 1. After homogenization, the samples were cut into smaller, $4 \times 4 \times 10$ mm pieces using a wire electrical discharge machine (EDM). The surfaces of the samples were ground to P1200 grit using SiC abrasive paper, cleaned in ethanol in an ultrasonic cleaner for 15 min, and weighed before oxidation.

2.2 | Oxidation

To isolate oxidation driven solely by oxygen diffusion and eliminate effects of nitridation, two atmospheres were employed: Ar-2.5 vol.%O_2 and Ar-5 vol.%H_2O. Thermodynamic equilibrium calculations using the software Factsage 5 [21]

TABLE 1 | Nominal compositions of the three different materials under investigation.

at.%	Ta	Mo	Cr	Ti	Al
Equiatomic alloy	20	20	20	20	20
Cr-rich alloy	20	20	26.7	13.3	20
Ti-rich alloy	20	20	13.3	26.7	20

show that the humid argon mixture corresponds to an oxygen partial pressure of approximately 1.2×10^{-6} bar at 1000°C. This pO_2 falls well inside the range in which chromia scales can volatilize in the presence of water vapor via formation of species such as $CrO_2(OH)_2$, a phenomenon documented for chromia-forming alloys in steam-containing environments [22, 23]. Consequently, the Ar–H_2O atmosphere not only reveals how humidity and possible proton incorporation affect oxide scale growth and morphology but also allows assessment of chromium loss by evaporation. All oxidation experiments were performed at 1000°C in the two atmospheres described above.

The samples were placed in alumina crucibles for isothermal oxidation and positioned in a tube furnace. The furnace was heated at a rate of 8 K/min up to 1000°C in Ar-5 vol.%H_2O and Ar-2.5 vol.%O_2 atmospheres with flow rate of 50 mL/min and a dwell time of 48 h. Samples were weighed after oxidation.

2.3 | Analysis

The oxide scales were investigated from the top surface using X-ray diffraction (Bruker D8, Cu x-ray tube) to determine the crystallographic structure of phases. The via cross-sections were analyzed using scanning electron microscopy (SEM, Hitachi FlexSEM & Hitachi SU5000) in backscatter electron mode (BSE), electron backscatter diffraction (EBSD) and energy dispersive X-ray spectroscopy (EDS), as well as electron probe micro analysis (EPMA, JEOL JXA 8100). The samples were mounted in epoxy resin and their surfaces were polished using up to P2400 grit SiC paper, 3 μm, 1 μm, and 20 nm polishing suspensions. To investigate the microstructure and chemical composition of the alloys before oxidation, non-oxidized samples were analyzed applying the same techniques. Phase fractions were determined via image processing software ImageJ.

3 | Results

3.1 | Initial Microstructure

The microstructure of the equiatomic Ta-Mo-Cr-Ti-Al alloy after homogenization consists of an ordered cubic B2 phase and a hexagonal C14 Laves phase identified by X-ray diffraction, as shown in Figure 1. The C14 phase forms on the grain boundaries and has a volume fraction of (2.9 ± 1.4) % as determined via image analysis from SEM-BSE images, see Figure 2. The average grain size, as determined by the line-intersection method, is (708 ± 235) μm. Even though there is a significant variation in grain size, the different sizes are evenly distributed throughout the sample, due to the heat treatment and slow
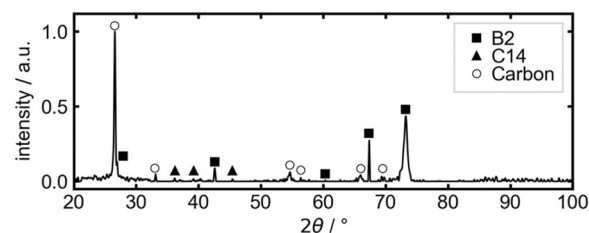

FIGURE 1 | XRD pattern of the equiatomic alloy before oxidation.

furnace cooling. The grain size distribution before the heat treatment step on the other hand shows a significant gradient due to the anisotropic cooling of the arc melters water cooled copper mold. The C14 phase consists primarily of Cr, Ta, and Al. The observed Ta-Mo-Cr-Ti-Al alloy microstructure is in accordance with other published works, e.g., in [13]. The nominal and experimentally determined chemical compositions of the alloy, and the element distribution in individual phases, as well as the phase fractions, are included in Table 2.

The alloy 20Ta-20Mo-27Cr-13Ti-20Al with a 2:1 Cr:Ti ratio exhibits the same B2 and C14 phases as the equiatomic alloy, as identified by XRD (Figure 3). Though, as can be observed in the BSE SEM micrograph in Figure 4, the C14 Laves phase is present not only at the grain boundaries, but also within the grains. The fraction of the C14 Laves phase is greater at (33.9 ± 2.1) %, compared to the equiatomic alloy (see Table 2). The differing Cr:Ti ratio did not significantly alter the chemical composition of the C14 phase, compared to the equiatomic

alloy; only the composition of the B2 phase differed, being richer in Ti and leaner in Mo. The grain size is reduced significantly to (73 ± 34) µm, compared to the equiatomic alloy.

The alloy 20Ta-20Mo-13Cr-27Ti-20Al with a 1:2 Cr:Ti ratio does not show X-ray diffraction peaks corresponding to the C14 phase (not shown), but single phase B2 material results. The SEM-BSE micrograph confirms this, as shown in Figure 5. The alloy appears
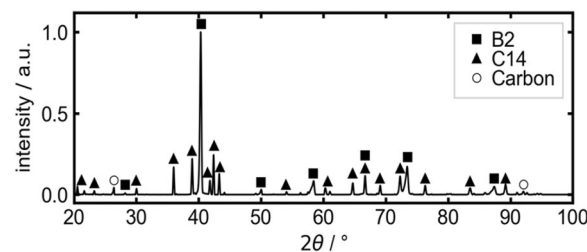
FIGURE 3 | XRD pattern of the Cr-rich alloy before oxidation.
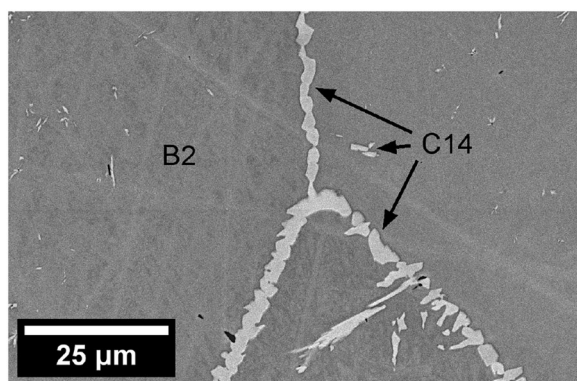
FIGURE 2 | SEM-BSE image of the equimolar alloy showing the B2 matrix and C14 Laves phase formed at the grain boundaries. Some scratches from the polishing procedure are visible, these are not part of the microstructure.
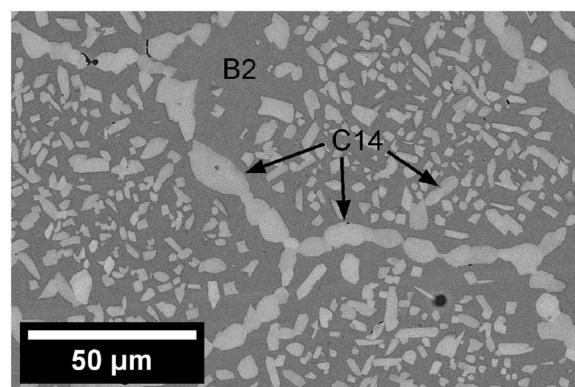
FIGURE 4 | SEM-BSE image of the 2:1 Cr:Ti Cr-rich alloy showing the B2 matrix and C14 Laves phase formed at the grain boundaries and within the B2 matrix.

TABLE 2 | Nominal and actual alloy compositions of the equimolar reference alloy Ta-Mo-Cr-Ti-Al, the Cr-rich and Ti-rich alloy and resulting phases and phase fractions.

| at.%	Ta	Mo	Cr	Ti	Al	Area fraction/%
Equiatomic alloy						
Nominal composition	20	20	20	20	20	—
Actual composition	19.2 ± 1.9	18.6 ± 2.9	20.4 ± 1.6	21.1 ± 3.0	20.8 ± 1.9	—
C14	27.1 ± 0.1	4.8 ± 0.1	46.3 ± 0.2	6.4 ± 0.1	15.3 ± 0.2	2.9 ± 1.4
B2	19.5 ± 0.2	18.8 ± 0.2	20.1 ± 0.2	21.1 ± 0.1	20.5 ± 0.1	97.1 ± 1.4
Cr-rich alloy						
Nominal composition	20	20	26.7	13.3	20	—
Actual composition	19.8 ± 0.6	19.5 ± 1.3	27.3 ± 1.6	13.6 ± 0.7	19.8 ± 0.5	—
C14	26.8 ± 0.5	7.0 ± 1.4	43.4 ± 1.8	5.8 ± 0.8	16.9 ± 0.3	33.9 ± 2.1
B2	16.4 ± 0.7	27.8 ± 1.3	15.5 ± 1.5	18.9 ± 0.7	21.4 ± 0.6	66.1 ± 2.1
Ti-rich alloy						
Nominal composition	20	20	13.3	26.7	20	—
Actual composition	20.0 ± 0.5	19.2 ± 0.5	13.0 ± 0.4	28.0 ± 0.6	19.8 ± 0.7	
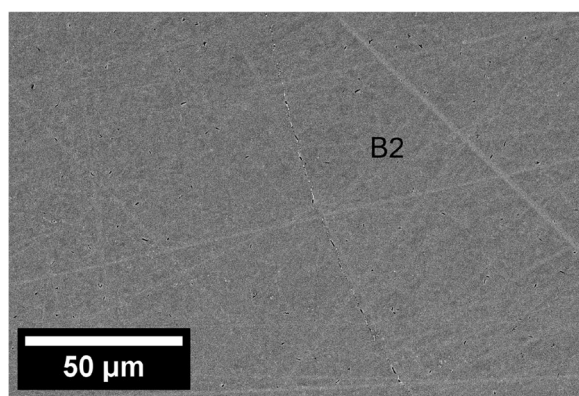
FIGURE 5 | SEM-BSE image of the 1:2 Cr:Ti Ti-rich alloy showing the B2 single phase microstructure. Some scratches from the polishing procedure are visible, these are not part of the microstructure.
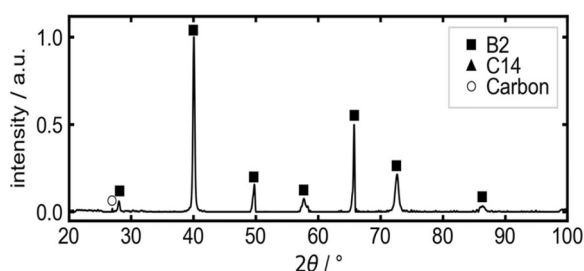
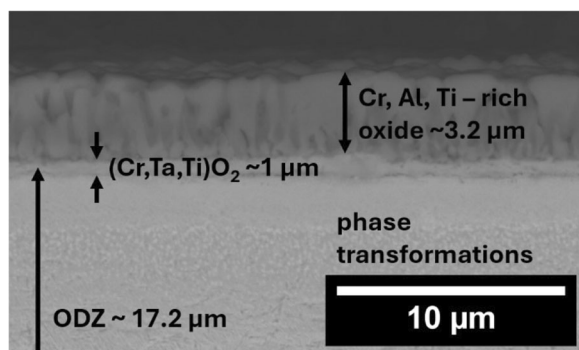**FIGURE 6** | XRD pattern of the Ti-rich alloy before oxidation.

FIGURE 7 | SEM-BSE image of the equiatomic alloy after oxidation for 48 h at 1000°C in Ar-2.5%O_2.

to be single-phase from SEM-BSE images, though the presence of C14 Laves phase was confirmed by XRD in Figure 6. The Ti-rich alloy chemical composition is included in Table 2.

3.2 | Oxidation Behavior in Ar-O_2

After 48 h at 1000°C, the equimolar alloy Ta-Mo-Cr-Ti-Al develops a mixed, columnar outer scale composed of titania, alumina and chromia as shown in Figure 7. The initial oxide islands must continue to grow outward in a columnar manner. EPMA maps (Figure 8) show that the Cr signal has a higher intensity deeper within the layered oxide than Ti and Al, and a (1.0 ± 0.1) μm-thick, continuous Cr-Ti-Ta oxide layer separates the outer heterogeneous scale from the substrate. This Cr-Ti-Ta oxide is also visible as a thin layer in the BSE micrograph (Figure 7). The total oxide thickness is (4.2 ± 0.2) μm, followed by an internal oxygen diffusion zone (ODZ) of (17.2 ± 1.0) μm. Below the scale, depletion of Cr, Al and Ti is evident. The ODZ occasionally contains bright precipitates, as seen in Figure 7. The precipitates show an increased Cr content in the EPMA maps and lower Ti content (Figure 8). The Cr-depleted region below the ODZ does not show any phase transformations. Below the Ti depleted region, a Ta richer region is visible within the ODZ which also correlates with a higher oxygen content in the ODZ. The BSE micrographs also show some internal oxidation in this region.

The higher 2:1 Cr:Ti alloy (20Ta-20Mo-27Cr-13Ti-20Al) exhibits a different morphology after 48 h at 1000°C. As seen in Figure 9,
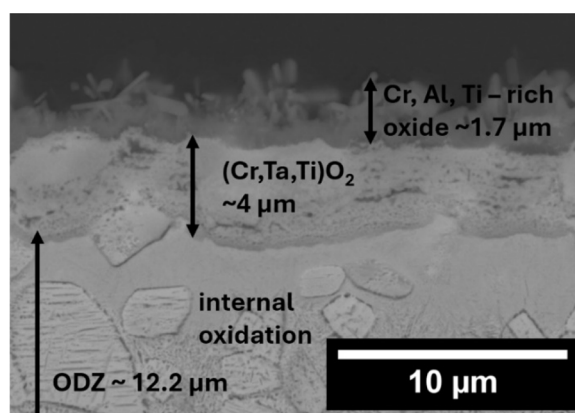
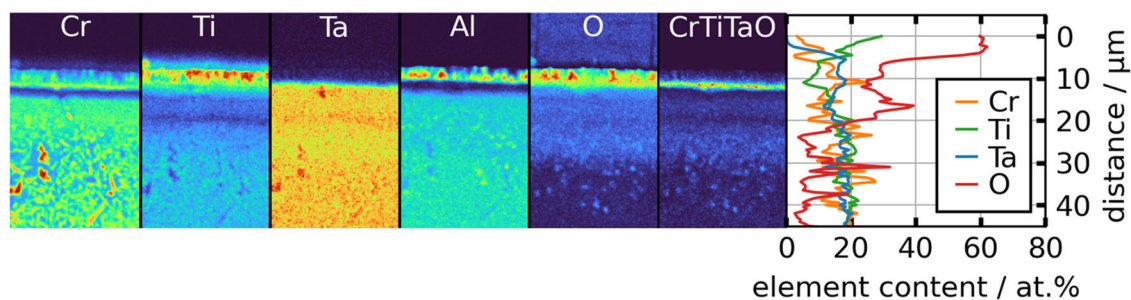**FIGURE 9** | SEM-BSE image of the 2:1 Cr:Ti Cr-rich alloy after oxidation for 48 h at 1000°C in Ar-2.5%O_2.

FIGURE 8 | EPMA elemental map of the equiatomic alloy after oxidation for 48 h at 1000°C in Ar-2.5%O_2, individual element maps and an overlay indicating the position of (Cr,Ti,Ta)O_2. The quantitative linescan displays the elemental composition through the middle of the maps. [Color figure can be viewed at wileyonlinelibrary.com]

the outer scale consists of discontinuous titania and alumina, whereas the underlying chromia layer is continuous. Beneath the chromia, an approximately (4.0 ± 0.3) μm-thick Cr-Ti-Ta oxide is present, although it is less sharply defined than in the equiatomic material. The overall oxide thickness is (5.7 ± 0.7) μm and the ODZ is (12.2 ± 2.4) μm as can be seen in the EPMA mapping in Figure 10. The ODZ is somewhat irregular, and isolated patches are not always connected to the main ODZ front, although they could be in the out-of-plane dimension. Some dark features inside the ODZ show internal oxidation. The Cr-depleted region within the ODZ shows no internal oxidation, while the rest of the ODZ shows a reduced Ti content.

The 1:2 Cr:Ti Ti-rich alloy (20Ta-20Mo-13Cr-27Ti-20Al) after 48 h at 1000°C forms an oxide architecture that visually resembles the equiatomic alloy as demonstrated in Figures 11 and 12. A non-continuous outer mixture of titania, alumina and chromia overlies a thinner, continuous Cr-Ti-Ta oxide of (2.0 ± 0.3) μm. The total external scale is (7.4 ± 0.7) μm and the ODZ extends to (21.6 ± 1.0) μm. Unlike the Cr-rich alloy, the ODZ is continuous, and internal oxidation is observed in the lower region of the ODZ. All alloys appear to dissolve around (30 ± 4) at.% of oxygen in the ODZ formed within the substrate.

3.3 | Oxidation in Ar-H₂O

The equiatomic alloy forms multiple oxide layers as part of the oxide scale, which forms after 48 h at 1000°C under Ar-5 vol.% H_2O, as can be seen in the SEM-BSE micrograph in Figure 13. Using the EPMA elemental maps in Figure 14, and quantitative linescans, it is possible to identify the positions of the different oxides within the complex scale. This alloy forms an outer non-continuous titania layer followed by a mixed alumina and chromia layer. The substrate below the oxide layers is depleted of Cr, Ti and Al. Overlaying the elemental maps of Cr, Ti, Ta and O, it is possible to identify the Cr-Ti-Ta-oxide within the oxide scale. In this case, the Cr-Ti-Ta-oxide forms a thin, continuous layer at the interface between the chromia and the substrate material. Both EPMA (Figure 14) and SEM (Figure 13) show a zone of oxygen diffusion and internal corrosion below the oxide scale. The thickness of this ODZ is (12.8 ± 0.8) μm with a total oxide scale thickness of (2.7 ± 0.5) μm. The inner $(Cr,Ti,Ta)O_2$ has a thickness of (0.4 ± 0.1) μm. In the Cr-depleted region just below the oxides, no phase

transformations are visible. Further within the alloy internal oxidation is visible in the ODZ which correlates with the Ta signal.

The SEM-BSE micrograph of the oxidized 2:1 Cr:Ti ratio alloy (20Ta-20Mo-27Cr-13Ti-20Al) shown in Figure 15 shows an oxide scale comparable to the equiatomic alloy after 48 h at 1000°C under Ar-5 vol.%H_2O. The quantitative EPMA measurements (Figure 16) show the same layering of oxides. As for the equiatomic alloy, the outer layer consists of non-continuous titania, with a mixed chromia and alumina layer underneath, where both inner oxides are continuous. The EPMA map overlays (Figure 16) identify a thin, continuous Cr-Ti-Ta-oxide located at the interface of the substrate and the outer oxide scale. The ODZ thickness is (18 ± 1.3) μm and the total oxide scale thickness is (3.4 ± 0.5) μm with the $(Cr,Ti,Ta)O_2$ having a thickness of (1.4 ± 0.3) μm. There are no phase transformations visible in the ODZ. There is internal oxidation within the ODZ which trends with the Ti signal and only appears below the Cr depleted regions just below the oxides. It is noteworthy that the Laves phase appears to dissolve only (20 ± 1) at.% of oxygen, compared to the B2 matrix which dissolves (30 ± 4) at.% oxygen, as determined by quantitative EPMA WDS measurements.

The 1:2 Cr:Ti ratio alloy 20Ta-20Mo-13Cr-27Ti-20Al has the same oxide morphology as both other alloys after oxidation (48 h at 1000°C under Ar-5 vol.%H_2O) as seen in Figure 17, except that the outer titania layer is significantly thicker and more continuous (EPMA maps of Figure 18), as compared to the other alloys. Chromia and alumina form thin and continuous oxides below the outer titania layer. The Cr-Ti-Ta oxide is
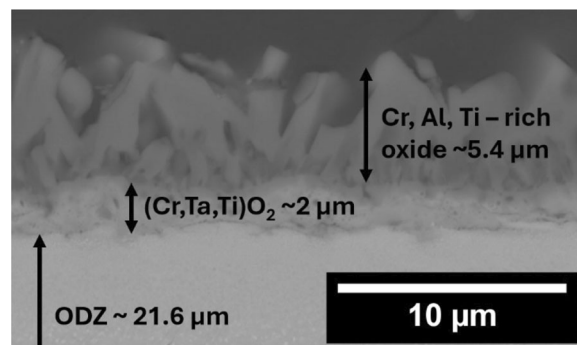

FIGURE 11 | SEM-BSE image of the 1:2 Cr:Ti Ti-rich alloy after oxidation for 48 h at 1000°C in Ar-2.5%O_2.
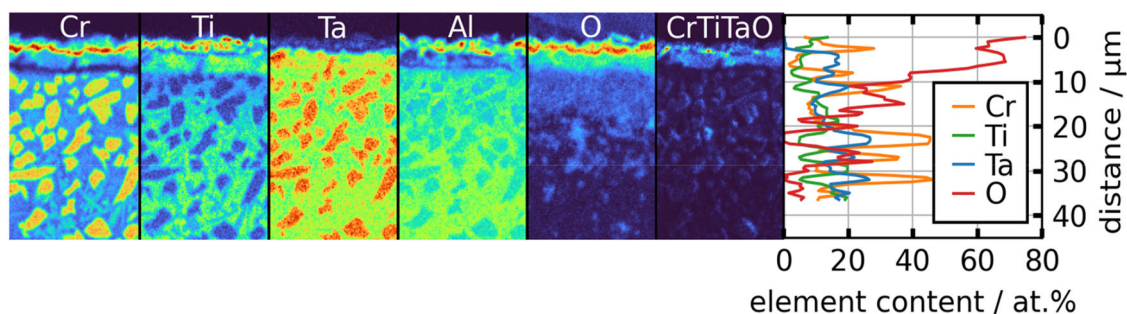

FIGURE 10 | EPMA elemental map of the 2:1 Cr:Ti Cr-rich alloy after oxidation for 48 h at 1000°C in Ar-2.5%O_2, individual element maps and an overlay indicating the position of $(Cr,Ti,Ta)O_2$ is shown. The quantitative linescan displays the elemental composition through the middle of the maps. [Color figure can be viewed at wileyonlinelibrary.com]
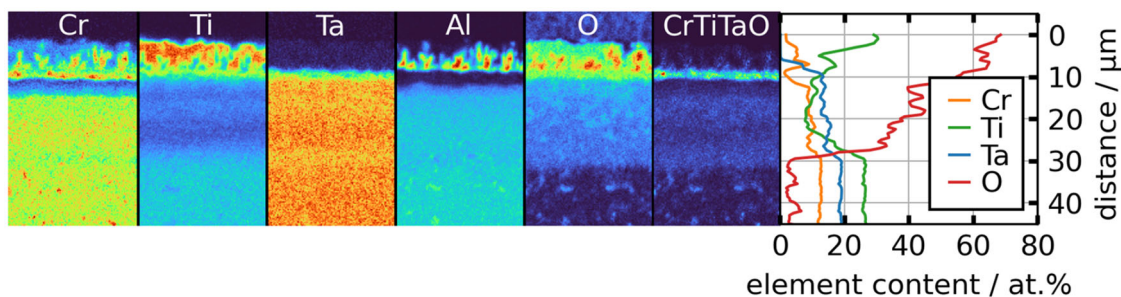
FIGURE 12 | EPMA elemental map of the 1:2 Cr:Ti Ti-rich alloy after oxidation for 48 h at 1000°C in Ar-2.5%O_2, individual element maps and an overlay indicating the position of $(Cr,Ti,Ta)O_2$ is shown. The quantitative linescan displays the elemental composition through the middle of the maps. [Color figure can be viewed at wileyonlinelibrary.com]
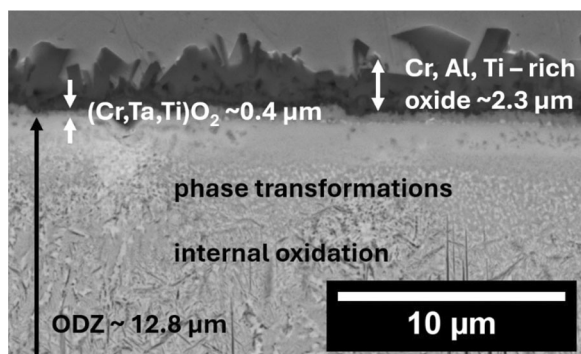

FIGURE 13 | SEM-BSE micrograph of the equiatomic alloy after oxidation for 48 h at 1000°C in Ar-5 vol.%H_2O.

again found at the substrate-oxide interface. The total oxide thickness is (5.1 ± 0.5) μm, followed by an ODZ with a thickness of (13.7 ± 0.7) μm, see Figure 18. The $(Cr,Ti,Ta)O_2$ has a thickness of (0.9 ± 0.1) μm. This alloy shows only a small band of precipitates below the Cr-depleted zone, followed by internal oxidation in the ODZ, correlating to the Ta signal. No precipitates or internal oxidation occurred in the Cr-depleted sub-surface zone.

4 | Discussion

4.1 | Oxidation Mechanisms in Ar-2.5 Vol.%O_2

The proposed defect equilibria hypothesis is based on the charge compensation mechanism in rutile-structured $(Cr,Ti,Ta)O_2$. In this oxide system, Ti^{4+} substitution for Cr^{3+} creates excess positive charge that must be compensated by reducing oxygen vacancy concentration.

This electronic compensation should theoretically reduce oxygen transport rates. However, the observed results contradict this simple defect model, suggesting that microstructural effects dominate over defect chemistry considerations. The increased Ti content not only affects the oxide defect structure but also alters the substrate microstructure (Table 2) and phase distribution which influence oxidation kinetics.

Contrary to the proposed hypothesis that an increased Ti to Cr ratio would lead to a reduced oxygen diffusion through the $(Cr,Ti,Ta)O_2$ scale, an increased ODZ was observed below the outer oxides (Figure 19). The ODZ thickness correlated directly to the Ti content, which reflects the high oxygen solubility of Ti, enabling deeper oxygen penetration into Ti-rich substrates compared to other alloying elements. As shown in Table 3, Ti can dissolve up to ~30 at.% oxygen in both α and β phases, creating a large oxygen-enriched zone that facilitates further inward diffusion, even at 1000°C.

The thickness of the outer oxides also correlates directly to the Ti content. Only the $(Cr,Ti,Ta)O_2$ layer is thicker on the 2:1 Cr:Ti **Cr-rich alloy**, perhaps due to the large amounts of Ti-lean Laves phase present in the substrate, leading to the hypothetical formation of a Ti-lean $(Cr,Ti,Ta)O_2$ or $(Cr,Ta)O_2$. Such Ti-lean oxides would theoretically be less protective and faster growing due to higher defect concentrations and reduced thermodynamic stability, as confirmed by equilibrium calculations with the software FactSage 5 [21]. Additionally, the higher Cr content should allow for more continuous chromia formation, acting as an additional protective barrier to oxygen diffusion, as shown in Figure 16. For the 1:2 Cr:Ti Ti-rich alloy, the quantitative EPMA analysis (Figure 18) shows a lower Cr content in the region where $(Cr,Ti,Ta)O_2$ forms, possibly even indicating the formation of a Cr-lean $(Cr,Ti,Ta)O_2$ or even Ti-TaO_4. However, thermodynamic calculations with the software Factsage 5 [21] suggest equiatomic $(Cr,Ti,Ta)O_2$ to be more stable than the Cr-free tantalate.

Different internal oxides appear to form within the ODZ of all three alloys. The **equiatomic alloy** serves as the reference system, showing characteristic internal Ta_2O_5 formation, as indicated by the correlation between Ta and O signals in Figure 8. This internal Ta oxidation correlates with the dark features observed in SEM (Figure 7) and could be detrimental due to the high Pilling-Bedworth ratio of Ta_2O_5 (PBR = 2.43) [28], creating mechanical stresses from volume expansion that can lead to oxide cracking. Additionally, fine precipitates appear below the oxide scale but above the internal oxidation zone. Based on BSE contrast matching and Cr enrichment, these are most likely Cr_2Ta C14 Laves phase precipitates that form due to local Cr supersaturation during oxidation.

The **Cr-rich alloy** shows distinctly different behavior. Phase transformations are largely absent, likely because the pre-existing 33.9% intragranular C14 Laves phase (Table 2) provides favorable nucleation sites, allowing precipitating phases to grow on existing grain boundaries rather than forming new fine
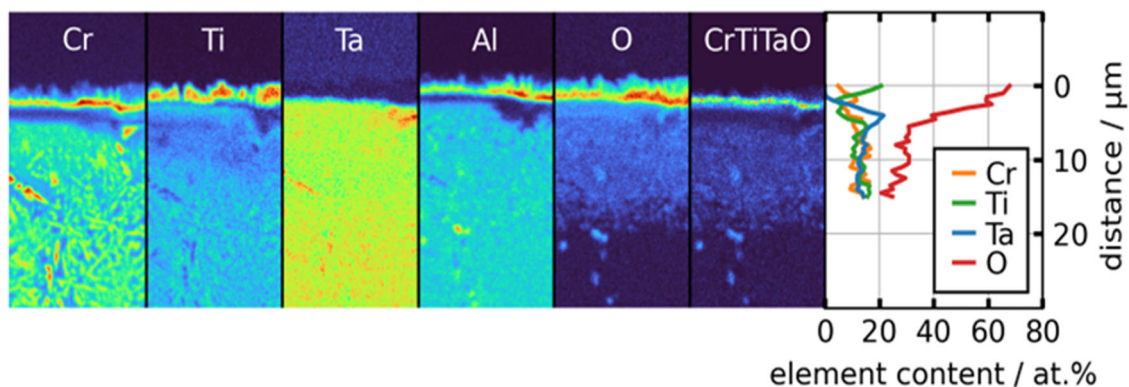
FIGURE 14 | EPMA WDS maps and linescans of the equiatomic alloy after oxidation for 48 h at 1000°C in Ar-5 vol.%H$_2$O. [Color figure can be viewed at wileyonlinelibrary.com]
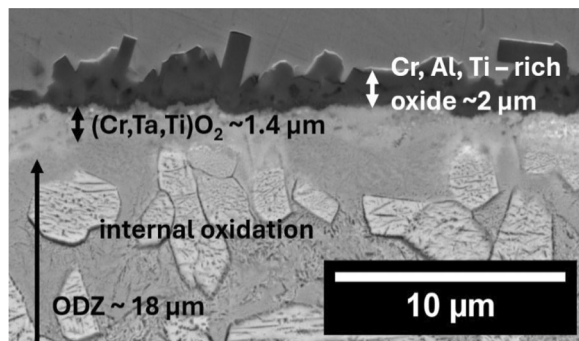

FIGURE 15 | SEM-BSE micrograph of the 2:1 Cr:Ti Cr-rich alloy after oxidation for 48 h at 1000°C in Ar-5 vol.%H$_2$O.

precipitations. The internal oxidation pattern also differs: instead of Ta-rich precipitates, the internal oxidation correlates with the Ti signal in EPMA maps (Figure 10), suggesting preferential internal TiO$_2$ formation below the Cr-depleted zone. This shift reflects the altered local chemistry due to the high C14 fraction.

The **Ti-rich alloy** exhibits the simplest internal behavior. Like the **Cr-rich alloy**, it forms internal TiO$_2$ (Ti-O signal correlation in Figure 12) but shows minimal phase transformations. This supports the conclusion that fine precipitates in other alloys are indeed Cr$_2$Ta C14 phases, as the reduced Cr content (13.3 at.%) limits their formation. Notably, this alloy develops the most defined and continuous ODZ due to the virtual absence of Laves phase barriers, enabling enhanced oxygen diffusion since the B2 matrix dissolves more oxygen (~30 at.%) than C14 phase (~20 at.%). The resulting morphologies are illustrated in Figure 20.

4.2 | Oxidation Mechanisms in Ar-5 Vol.%H$_2$O

For oxidation under Ar-5 vol.%H$_2$O at 1000°C after 48 h, the results show improved performance with higher Ti content, but the underlying mechanisms are more complex than simple defect chemistry predictions. While ODZ thickness inversely correlates with Cr:Ti ratio (Figure 21), this improvement results from multiple competing.

The improved performance of **Ti-rich alloy** in humid conditions can be attributed to several factors. While Cr evaporation through CrO$_2$(OH)$_2$ formation is well-documented for pure

chromia scales [22, 23], its relevance to our mixed oxide scales requires careful consideration. In our system, the outer chromia layer is discontinuous and mixed with titania and alumina, potentially reducing the effective Cr activity and thus limiting volatilization rates compared to pure chromia systems. The water vapor containing atmosphere led to thinner and more compact chromia on all alloys (Figures 13, 15, and 17). According to the EPMA maps (Figures 14, 16, and 18), the (Cr,Ti,Ta)O$_2$ appears to form thinner and denser layers under Ar-5 vol.%H$_2$O atmosphere, indicating that the protection of the individual oxides, especially chromia, is significantly reduced under water vapor.

While the internal oxidation morphology appears similar between atmospheres, the ODZ thickness data (Figure 19 vs. Figure 21) reveals important quantitative differences. In Ar-H$_2$O, all alloys show altered ODZ thickness compared to Ar-O$_2$: **equiatomic** (12.8 vs. 17.2 μm), **Cr-rich** (18.0 vs. 12.2 μm), and **Ti-rich** (13.7 vs. 21.6 μm). Quantitative analysis shows that the **Ti-rich alloy** achieves a 37% thinner ODZ (13.7 vs. 21.6 μm) compared to their performance in Ar-O$_2$, while the **Cr-rich alloy** shows increased ODZ thickness (18.0 vs. 12.2 μm), demonstrating opposite trends between alloy compositions.

The different oxygen diffusion behavior of the alloys in the different atmospheres is explained by the higher hydrogen uptake of Ti in the **Ti-rich** and **equimolar alloys** compared to the **Cr-rich alloy**. Ti has high hydrogen solubility and forms stable hydrides [29, 30], potentially reducing oxygen diffusion through competitive site occupation or altered electronic structure. This hydrogen uptake could potentially reduce oxygen solubility in the matrix and lead to reduced oxygen diffusion, explaining the reduced ODZ thickness in the **Ti-rich alloy** under humid conditions.

Considering the substantially lower oxygen partial pressure (1.2 × 10^{-6} bar at 1000°C) in the Ar-5 vol.%H$_2$O atmosphere compared to ~0.025 bar in Ar-2.5 vol.%O$_2$, the hydrogen influence appears more significant than that of oxygen supply. The correlation between atmosphere and ODZ thickness suggests different rate-limiting mechanisms: in dry O$_2$, oxygen supply is abundant and substrate transport controls kinetics, while in humid conditions, oxide scale properties or hydrogen interference may become rate-limiting.

Independent of hydrogen effects, the precipitation behavior supports identification of fine precipitates as Cr$_2$Ta C14 Laves
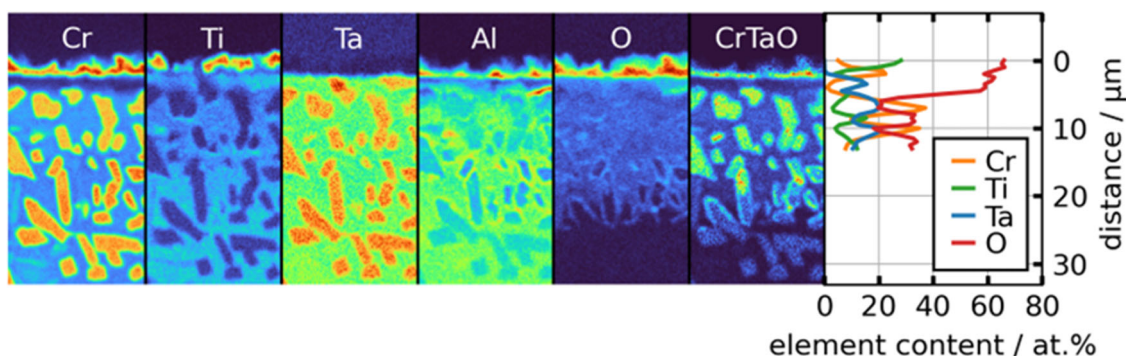
FIGURE 16 | EPMA WDS maps and linescans of the 2:1 Cr:Ti Cr-rich alloy after oxidation for 48 h at 1000°C in Ar-5 vol.%H$_2$O. [Color figure can be viewed at wileyonlinelibrary.com]
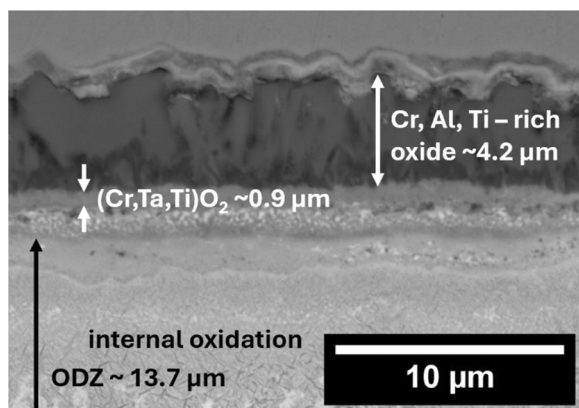

FIGURE 17 | SEM-BSE micrograph of the 1:2 Cr:Ti Ti-rich alloy after oxidation for 48 h at 1000°C in Ar-5 vol.%H$_2$O.

phase. The ODZ morphologies appear similar to those in the Ar-2.5 vol.%O$_2$ atmosphere, forming few precipitates in the **Ti-** and **Cr-rich alloys**, while a significant number of precipitates are evident for the **equiatomic alloy**. These precipitates form preferentially in high-Cr regions but are suppressed in the **Ti-rich alloy** due to reduced Cr availability, creating different diffusion path networks.

The higher content of the C14 Laves phase for the **Cr-rich alloy** (Table 2) and the increased grain boundary density (smaller grain size) might enable grain boundary diffusion of oxygen and thus increased oxygen diffusion, which is in line with the findings of [28, 29, 31–33]. It is noteworthy that the Laves phase appears to dissolve only ~20 at.% of oxygen, compared to the B2 matrix which dissolves ~30 at.% oxygen, as determined by quantitative EPMA WDS measurements.

The superior performance of the **Ti-rich alloy** in humid conditions likely results from both chemical effects (hydrogen uptake reducing oxygen transport) and microstructural effects (absence of Laves phase barriers enabling more uniform element distribution). The water vapor exposure provides a more significant indication of the protectiveness of the (Cr,Ti,Ta)O$_2$, as the tantalate in this case is not covered by an outer continuous chromia layer and must provide the primary protection.

In all ODZs of all three alloys after exposure under Ar-5 vol.%H$_2$O, the Ta signal matches the regions of internal oxidation (Figures 14, 16, and 18), suggesting that dissolved oxygen preferentially oxidizes Ta in both the B2 and C14 Laves phases, especially in the case of the **Cr-rich alloy**. The resulting oxide layers, ODZs, precipitations and internal oxidation behavior for all three alloys under Ar-5 vol.%H$_2$O are summarized in Figure 22.

The different oxide morphologies between the Ar-2.5 vol.%O$_2$ and Ar-5 vol.%H$_2$O atmospheres indicate substantial influence of both hydrogen incorporation and modified oxide scale chemistry under humid conditions, demonstrating the complex interplay between atmospheric composition, alloy microstructure, and oxidation mechanisms.

5 | Conclusions

- In an Ar-2.5 vol.%O$_2$ atmosphere, the oxidation behavior showed an inverse correlation with the Cr:Ti ratio and resulting oxidation resistance:
  - Alloys with higher Cr content formed thinner ODZs and more continuous chromia layers, possibly demonstrating improving oxidation resistance.
  - The alloy with the highest Ti content formed a thicker ODZ, indicating greater inward oxygen diffusion, contrary to the initial hypothesis, possibly due to higher oxygen solubility in the matrix and formation of less protective Ti-rich tantalate or TiTaO$_4$.
  - A continuous Cr-Ta-Ti oxide layer was observed in all alloys but varied in thickness and density depending on composition.

- In an Ar-5 vol.%H$_2$O atmosphere, the oxidation behavior aligned more closely with the expected trends of improved oxidation resistance with a lower Cr:Ti ratio:
  - Alloys with higher Ti content exhibited thinner ODZs and thinner Cr-Ta-Ti oxide layers, while the chromia scales appeared denser as compared to Ar-2.5 vol.%O$_2$.
  - The outer titania scale was more pronounced for the Ti-rich alloys, but chromia and alumina were thinner and more continuous across all compositions.
  - The protective role of the (Cr,Ti,Ta)O$_2$ layer was more evident in humid conditions (Ar-5 vol.%H$_2$O) as the ODZ thickness directly correlates with the (Cr,Ti,Ta)O$_2$ thickness.
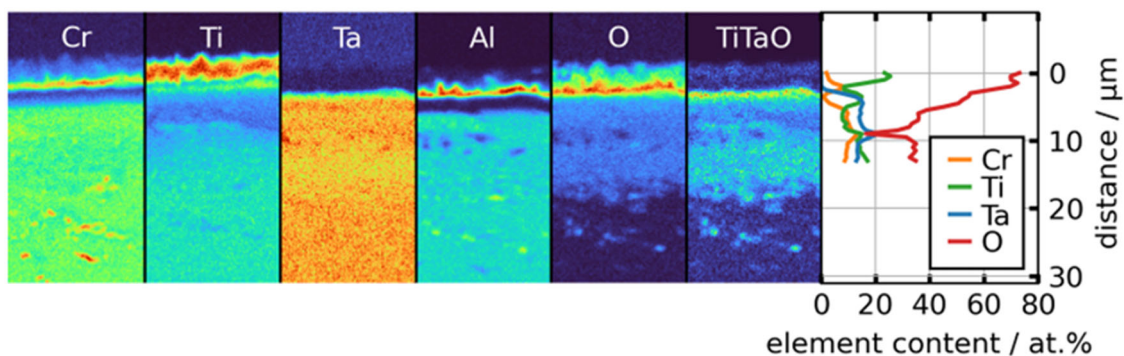
FIGURE 18 | EPMA WDS maps and linescans of the 1:2 Cr:Ti Ti-rich alloy after oxidation for 48 h at 1000°C in Ar-5 vol.%H$_2$O. [Color figure can be viewed at wileyonlinelibrary.com]
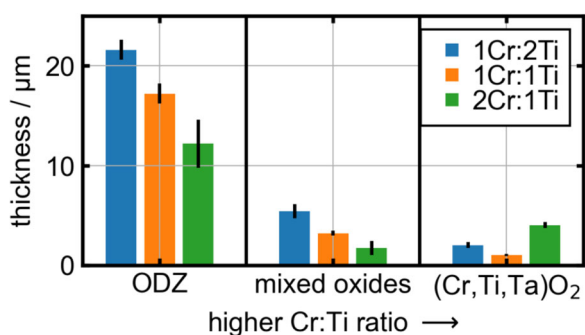

FIGURE 19 | Thicknesses of the different alloys ODZs, outer oxides and (Cr,Ti,Ta)O$_2$ scales after oxidation for 48 h at 1000°C in Ar-2.5 vol.% O$_2$. [Color figure can be viewed at wileyonlinelibrary.com]
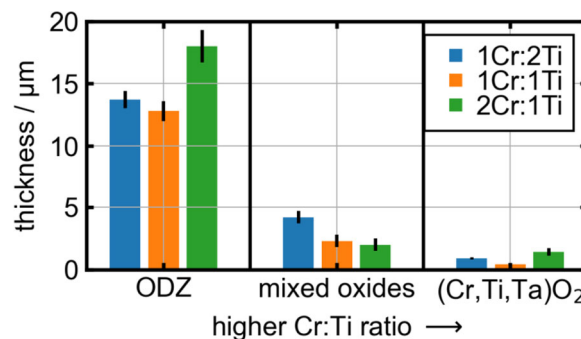

FIGURE 21 | Thicknesses of the different alloy ODZs, outer oxides and (Cr,Ti,Ta)O$_2$ scales after oxidation in Ar-5 vol.%H$_2$O for 48 h at 1000°C. [Color figure can be viewed at wileyonlinelibrary.com]

TABLE 3 | Oxygen solubility in pure elements at 1000°C [24–27].

Element	Ta	Mo	Cr	α-Ti	β-Ti
O solubility/at.%	3	0.03	< 0.002	33.3	< 2

FIGURE 20 | Illustration of the oxide morphologies of the different alloys after oxidation in the Ar-2.5 vol.%O$_2$ atmosphere for 48 h at 1000°C. The alloys are ordered from Ti-rich on the left, equiatomic in the middle to Cr-rich on the right. [Color figure can be viewed at wileyonlinelibrary.com]
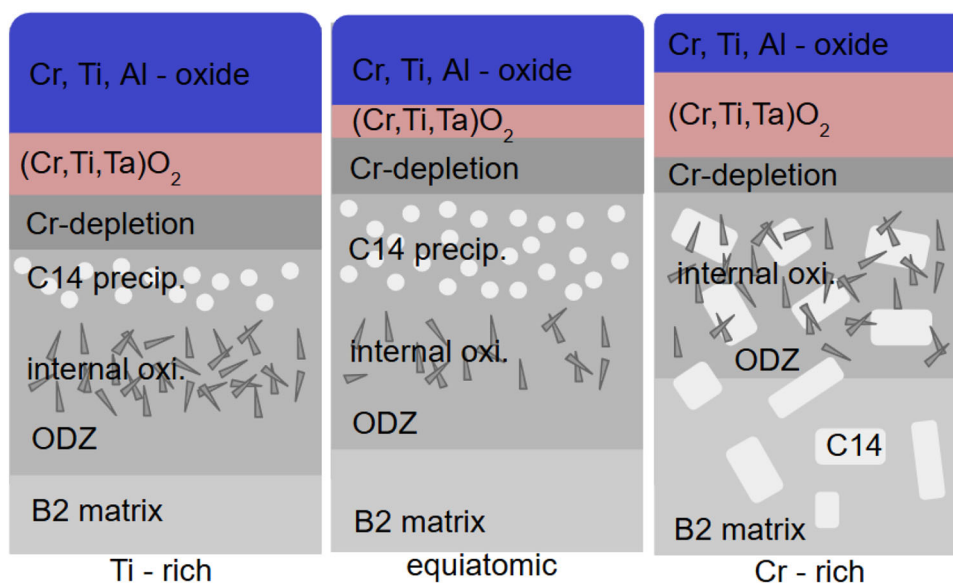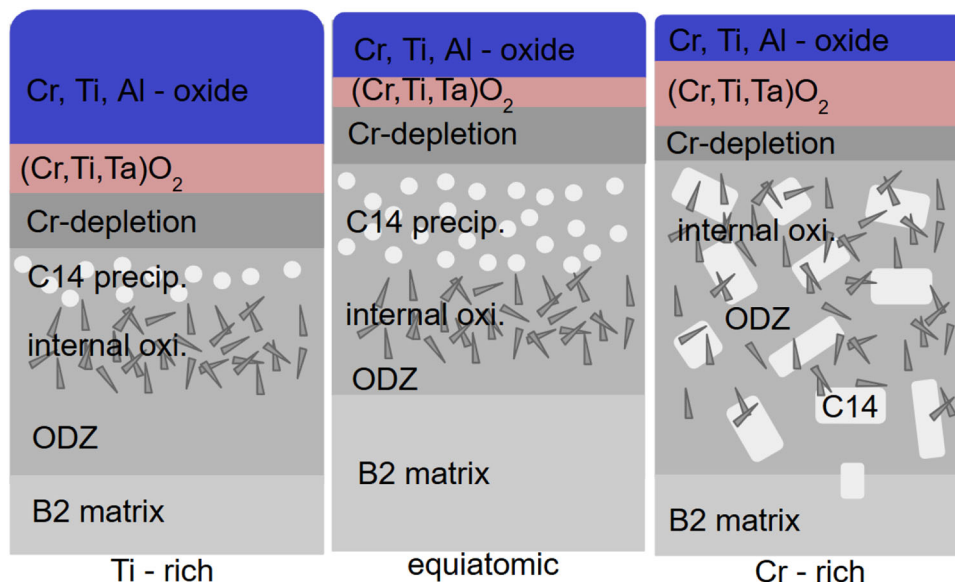
FIGURE 22 | Illustration of the oxide morphologies of the different alloys after oxidation in the Ar-5 vol.%H$_2$O atmosphere after 48 h at 1000°C. The alloys are ordered from Ti-rich on the left, equiatomic in the middle to Cr-rich on the right. [Color figure can be viewed at wileyonlinelibrary.com]

- The presence and fraction of the C14 Laves phase increased with Cr content, potentially enhancing grain boundary diffusion and oxidation.
- Overall, this study highlights the complex interplay between Cr and Ti in scale formation and oxidation behavior, especially in differing atmospheres:
  - Cr-rich alloys benefit from chromia stability in dry oxygen.
  - Ti-rich alloys show better performance in humid environments, possibly due to lower protectiveness by the outer chromia due to Cr volatilization, or via reduced oxygen diffusion and solubility through hydrogen uptake in the Ti rich alloys.

Conflicts of Interest

The authors declare no conflicts of interest.

Data Availability Statement

The data that support the findings of this study are available from the corresponding author upon reasonable request.

References

1. N. J. Welch, M. J. Quintana, T. M. Butler, and P. C. Collins, "High-Temperature Oxidation Behavior of TaTiCr, Ta4Ti3Cr, Ta2TiCr, and Ta4-TiCr3 Concentrated Refractory Alloys," *Journal of Alloys and Compounds* 941 (2023): 169000, https://doi.org/10.1016/j.jallcom.2023.169000.

2. N. J. Welch, M. J. Quintana, S. J. Kuhr, T. M. Butler, and P. C. Collins, "Intermediate and High-Temperature Oxidation Behavior of an Equiatomic TaTiCr RCCA From 800°C to 1400°C," *International Journal of Refractory Metals and Hard Materials* 118 (2024): 106437, https://doi.org/10.1016/j.ijrmhm.2023.106437.

3. B. Gorr, F. Müller, S. Schellert, et al., "A New Strategy to Intrinsically Protect Refractory Metal Based Alloys at Ultra High Temperatures," *Corrosion Science* 166 (2020): 108475, https://doi.org/10.1016/j.corsci.2020.108475.

4. O. N. Senkov, G. B. Wilks, D. B. Miracle, C. P. Chuang, and P. K. Liaw, "Refractory High-Entropy Alloys," *Intermetallics* 18, no. 9 (2010): 1758–1765, https://doi.org/10.1016/j.intermet.2010.05.014.

5. O. N. Senkov, G. B. Wilks, J. M. Scott, and D. B. Miracle, "Mechanical Properties of Nb25Mo25Ta25W25 and V20Nb20Mo20Ta20W20 Refractory High Entropy Alloys," *Intermetallics* 19, no. 5 (2011): 698–706, https://doi.org/10.1016/j.intermet.2011.01.004.

6. D. B. Miracle and O. N. Senkov, "A Critical Review of High Entropy Alloys and Related Concepts," *Acta Materialia* 122 (2017): 448–511, https://doi.org/10.1016/j.actamat.2016.08.081.

7. X. Xie, N. Li, W. Liu, et al., "Research Progress of Refractory High Entropy Alloys: A Review," *Chinese Journal of Mechanical Engineering* 35, no. 1 (2022): 142, https://doi.org/10.1186/s10033-022-00814-0.

8. J.-P. Couzinié, O. N. Senkov, D. B. Miracle, and G. Dirras, "Comprehensive Data Compilation on the Mechanical Properties of Refractory High-Entropy Alloys," *Data in Brief* 21 (2018): 1622–1641, https://doi.org/10.1016/j.dib.2018.10.071.

9. K. C. Atli and I. Karaman, "A Short Review on the Ultra-High Temperature Mechanical Properties of Refractory High Entropy Alloys," *Frontiers in Metals and Alloys* 2 (2023): 1135826, https://doi.org/10.3389/ftmal.2023.1135826.

10. F. Müller, B. Gorr, H.-J. Christ, H. Chen, A. Kauffmann, and M. Heilmaier, "Effect of Microalloying With Silicon on High Temperature Oxidation Resistance of Novel Refractory High-Entropy Alloy Ta-Mo-Cr-Ti-Al," *Materials at High Temperatures* 35, no. 1–3 (2018): 168–176, https://doi.org/10.1080/09603409.2017.1389115.

11. B. Gorr, F. Müller, M. Azim, et al., "High-Temperature Oxidation Behavior of Refractory High-Entropy Alloys: Effect of Alloy Composition," *Oxidation of Metals* 88, no. 3–4 (2017): 339–349, https://doi.org/10.1007/s11085-016-9696-y.

12. S. Schellert, B. Gorr, S. Laube, A. Kauffmann, M. Heilmaier, and H. J. Christ, "Oxidation Mechanism of Refractory High Entropy Alloys Ta-Mo-Cr-Ti-Al With Varying Ta Content," *Corrosion Science* 192 (2021): 109861, https://doi.org/10.1016/j.corsci.2021.109861.

13. F. Müller, B. Gorr, H. J. Christ, et al., "On the Oxidation Mechanism of Refractory High Entropy Alloys," *Corrosion Science* 159 (2019): 108161, https://doi.org/10.1016/j.corsci.2019.108161.

14. S. Schellert, M. Weber, H. J. Christ, et al., "Formation of Rutile (Cr,Ta,Ti)O2 Oxides During Oxidation of Refractory High Entropy Alloys in Ta-Mo-Cr-Ti-Al System," *Corrosion Science* 211 (2023): 110885, https://doi.org/10.1016/j.corsci.2022.110885.

15. S. Schellert, B. Gorr, H. Christ, et al., "The Effect of Al on the Formation of a CrTaO4 Layer in Refractory High Entropy Alloys Ta-Mo-Cr-Ti-xAl," *Oxidation of Metals* 96, no. 3–4 (2021): 333–345, https://doi.org/10.1007/s11085-021-10046-7.

16. W. Ren, F. Ouyang, B. Ding, et al., "The Influence of CrTaO4 Layer on the Oxidation Behavior of a Directionally-Solidified Nickel-Based Superalloy at 850–900°C," *Journal of Alloys and Compounds* 724 (2017): 565–574, https://doi.org/10.1016/j.jallcom.2017.07.066.

17. Z. Wu, W.-J. Yin, B. Wen, D. Ma, and L.-M. Liu, "Oxygen Vacancy Diffusion in Rutile TiO2: Insight From Deep Neural Network Potential Simulations," *Journal of Physical Chemistry Letters* 14, no. 8 (2023): 2208–2214, https://doi.org/10.1021/acs.jpclett.2c03827.

18. R. Schaub, E. Wahlström, A. Rønnau, E. Lægsgaard, I. Stensgaard, and F. Besenbacher, "Oxygen-Mediated Diffusion of Oxygen Vacancies on the TiO2(110) Surface," *Science* 299, no. 5605 (2003): 377–379, https://doi.org/10.1126/science.1078962.

19. M. Elahifard, M. R. Sadrian, A. Mirzanejad, R. Behjatmanesh-Ardakani, and S. Ahmadvand, "Dispersion of Defects in TiO2 Semi-conductor: Oxygen Vacancies in the Bulk and Surface of Rutile and Anatase," *Catalysts* 10, no. 4 (2020): 397, https://doi.org/10.3390/catal10040397.

20. N. J. Welch, T. M. Butler, M. J. Quintana, and P. C. Collins, "The Influence of Microstructure on the Oxidation Behavior of a TaTiCr Refractory Complex Concentrated Alloy," *Journal of Alloys and Compounds* 1003 (2024): 175613, https://doi.org/10.1016/j.jallcom.2024.175613.

21. C. W. Bale, E. Bélisle, P. Chartrand, et al., "Reprint of: Factsage Thermochemical Software and Databases, 2010–2016," *Calphad* 55 (2016): 1–19, https://doi.org/10.1016/j.calphad.2016.07.004.

22. E. J. Opila, "Volatility of Common Protective Oxides in High-Temperature Water Vapor: Current Understanding and Unanswered Questions," *Materials Science Forum* 461–464 (2004): 765–774, https://doi.org/10.4028/www.scientific.net/MSF.461-464.765.

23. D. J. Young and B. A. Pint, "Chromium Volatilization Rates From Cr2O3 Scales Into Flowing Gases Containing Water Vapor," *Oxidation of Metals* 66, no. 3–4 (2006): 137–153, https://doi.org/10.1007/s11085-006-9030-1.

24. W. D. Klopp, "Recent Developments in Chromium and Chromium Alloys," *JOM* 21, no. 11 (1969): 23–32, https://doi.org/10.1007/BF03378794.

25. H. Okamoto, "O-Ti (Oxygen-Titanium)," *Journal of Phase Equilibria and Diffusion* 32, no. 5 (2011): 473–474, https://doi.org/10.1007/s11669-011-9935-5.

26. B. Öztürk, M. Rudolphi, E. M. H. White, D. Dickes, U. Glatzel, and M. C. Galetz, "Influence of Water Vapor on the Oxidation of Pure Titanium," *High Temperature Corrosion of Materials* 101, no. 6 (2024): 1341–1351, https://doi.org/10.1007/s11085-024-10288-1.

27. B. Gorr, S. Schellert, F. Müller, H.-J. Christ, A. Kauffmann, and M. Heilmaier, "Current Status of Research on the Oxidation Behavior of Refractory High Entropy Alloys," *Advanced Engineering Materials* 23, no. 5 (2021): 1–14, https://doi.org/10.1002/adem.202001047.

28. S. Lu, X. Li, X. Liang, W. Yang, and J. Chen, "Effect of V and Ti on the Oxidation Resistance of WMoTaNb Refractory High-Entropy Alloy at High Temperatures," *Metals* 12, no. 1 (2022): 41, https://doi.org/10.3390/met12010041.

29. M. V. Chepak-Gizbrekht and A. G. Knyazeva, "Oxidation of TiAl Alloy by Oxygen Grain Boundary Diffusion," *Intermetallics* 162 (2023): 107993, https://doi.org/10.1016/j.intermet.2023.107993.

30. S. Ma, S.-D. Huang, Y.-H. Fang, and Z.-P. Liu, "TiH Hydride Formed on Amorphous Black Titania: Unprecedented Active Species for Photocatalytic Hydrogen Evolution," *ACS Catalysis* 8, no. 10 (2018): 9711–9721, https://doi.org/10.1021/acscatal.8b03077.

31. A. Katsman, H. J. Grabke, and L. Levin, "Penetration of Oxygen Along Grain Boundaries During Oxidation of Alloys and Inter-metallics," *Oxidation of Metals* 46, no. 3–4 (1996): 313–331, https://doi.org/10.1007/BF01050802.

32. C. Herzig and S. Divinski, "Bulk and Grain Boundary Diffusion in Intermetallic Compounds." *Diffusion Processes in Advanced Technological Materials* (Elsevier, 2005), 173–238.

33. M. Vaidya, K. G. Pradeep, B. S. Murty, G. Wilde, and S. V. Divinski, "Radioactive Isotopes Reveal a Non Sluggish Kinetics of Grain Boundary Diffusion in High Entropy Alloys," *Scientific Reports* 7, no. 1 (2017): 12293, https://doi.org/10.1038/s41598-017-12551-9.